Int. J. Electrochem. Sci., 16 **(2021)**, Article Number: 211252, doi: 10.20964/2021.12.47

International Journal of
ELECTROCHEMICAL
SCIENCE
www.electrochemsci.org

Short Communication

Study on the Electrochemical Mechanism of the Comprehensive Recovery of Valuable Components from Spent Cemented Carbide

Hongguang Kang, Jidong Li[*], *Jinlin Lu, Qian Wang, Yiyong Wang, Zhe Ning*

School of Materials and Metallurgy, University of Science and Technology Liaoning, Anshan 114051, China
[*]E-mail: lijidong2009@ustl.edu.cn

Received: 27 August 2020 / *Accepted:* 25 October 2020 / *Published:* 10 November 2021

Spent cemented carbide contains a large number of valuable metals including tungsten and cobalt. To reasonably and effectively utilize the secondary resources of spent cemented carbide, Co and WO_3 were recovered from spent cemented carbide by a combination of low-temperature electrochemical separation and high-temperature calcination. In a low-temperature (298 K) aqueous acid solution, a three-electrode system was used for electrochemical testing. The results show that on stainless steel cathodes, the deposition potential of Co(II) was between -0.6 and -0.5 V (vs SCE). Electrodeposition was controlled by diffusion and was irreversible. The diffusion coefficient of Co(II) was 7.12×10^{-7} cm^2 S^{-1}. The electrodeposition products were characterized by XRD and SEM, and the results showed that anode mud H_2WO_4 formed an orthorhombic crystal system. This H_2WO_4 was decomposed into WO_3 by high-temperature calcination. The combination of low-temperature electrochemical separation and high-temperature calcination thus serves as an effective way to recover and separate valuable metals from spent alloys.

Keywords: Spent cemented carbides; Recovery; WO_3; Cyclic voltammetry; Number of transferred electrons

1. INTRODUCTION

The nonferrous metals tungsten and cobalt are extremely important strategic resources and are the primary components of spent cemented carbide [1-2]. Spent cemented carbide accumulates, as it is used in many aspects of life [3]. Thus, the development of electrochemical methods for the recycling of spent cemented carbide is urgently needed.

There are currently many methods for recycling spent cemented carbides. However, all of these methods destroy the cobalt skeleton during recycling [4-5]. Compared with other methods,

electrochemical technology is more promising because of its simplicity, high current efficiency, high product purity, low environmental pollution, and high operability [6]. As an example, tungsten exists in the electrolyte in the forms of WC and H_2WO_4, and it has been treated as waste. This practice has caused considerable economic losses and environmental pollution [7].

To further examine the discharge mechanism of cobalt in spent cemented carbide, this study supplements our previous work on the number of transferred electrons and the electron transfer coefficient [8]. It is well known that the hydrogen discharge potential is more positive than that of cobalt. However, in acidic aqueous solutions, Co(II) can be discharged at the stainless steel cathode to obtain Co by controlling the electrodeposition process based on the Nernst equation [9]. At the same time, H_2WO_4 is enriched at the dissolvable spent cemented carbide anode, and it can be calcined into WO_3, as discovered through further research. However, this method has rarely been reported, and related electrochemical behavior can guide the recovery and separation of other valuable metals from spent alloys.

2. MATERIALS AND METHOD

Before the experiment, a stainless steel sample was polished with sandpaper of different grit sizes to make it bright, electrochemically degreased in an alkaline solution, and then ultrasonically cleaned with alcohol (25 °C, 10 min) and deionized water (25 °C, 5 min). The $CoCl_2 \cdot 6H_2O$ and H_3BO_3 used in the experiment were obtained from the Sinopharm Chemical Reagent Co., Ltd. with the expected purity (AR). H_2WO_4 was produced by the oxidation of WC.

In the experiment, a 300 mL solution containing 0.25 mol/L $CoCl_2 \cdot 6H_2O$ and 0.3 mol/L H_3BO_3 was used as the electrolyte. Spent cemented carbide was used as the anode, stainless steel was used as the cathode (the actual working area of both was 6 cm^2), and the two electrodes were placed opposite each other. At a current density of 40 mA/cm^2, high-purity Co was reduced at the cathode, and H_2WO_4 was simultaneously enriched at the anode with the oxidation of WC. High-purity WO_3 was obtained after the anode mud H_2WO_4 was recovered, washed, filtered, dried, ground, and calcined from 500 to 740 °C. The reaction process is shown in Fig. 1.

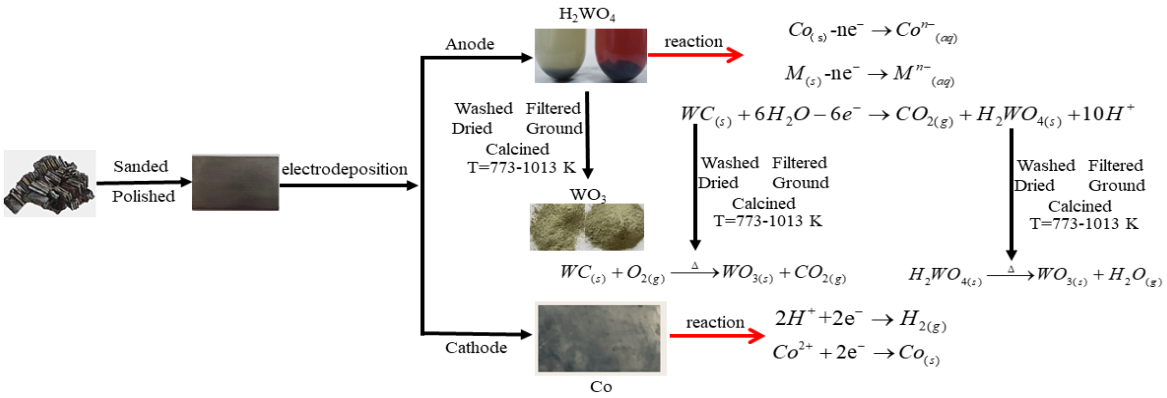

Figure 1. Reaction process

3. RESULTS AND DISCUSSION

3.1. Cyclic voltammetry analysis

To comprehensively study the electrochemical reactions and their mechanisms in the electrode system [10-11], cyclic voltammetry was carried out at 298 K over a scanning range from 100 to 120 mV/s in an electrolyte solution containing 0.05 mol/L $CoCl_2 \cdot 6H_2O$. A three-electrode system was used. The working electrode was stainless steel (S=0.785 cm^2), the reference electrode was a SCE, and the auxiliary stage was platinum (S=8 cm^2). The results are shown in Fig. 2.

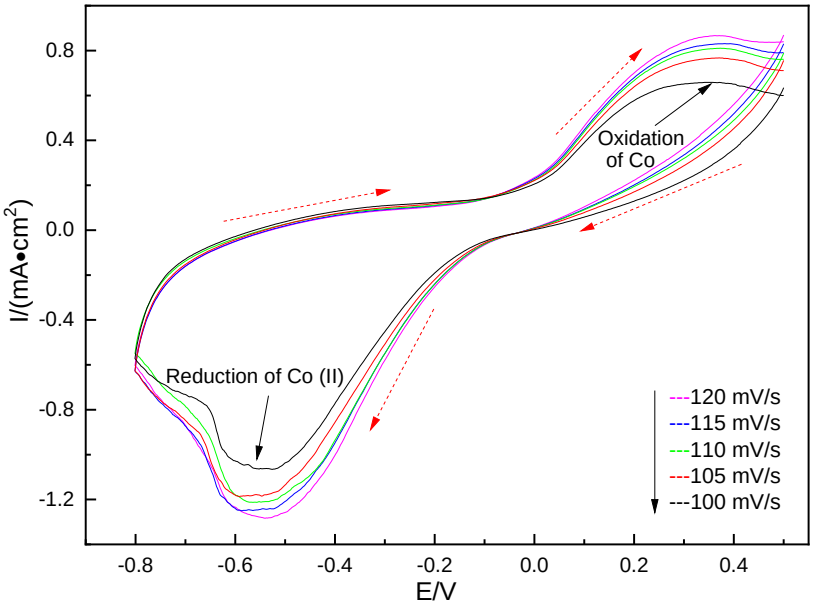

Figure 2. Cyclic voltammetry curve on a stainless steel electrode at 298 K using an electrolyte solution containing a Co(II) concentration of 0.05 mol/L and a scanning rate of 100-120 mV/s

As shown in Fig. 2, the electrochemical potential ranged from -0.8 to 0.5 V. Both an oxidation peak and a reduction peak were observed in the cyclic voltammetry curves during different scans, corresponding to the reduction of Co(II) and oxidation of Co, respectively. The reduction potential was -0.52 to -0.55 V. This value is close to the Co(II) (vs SCE) potential of -0.55 V obtained from the tables of standard electrode potentials. The oxidation potential was 0.35 to 0.39 V.

Cobalt is close to hydrogen in the metal active order, and H(I) inhibits the deposition of Co(II). However, increasing the Co(II) concentration increased its deposition potential to achieve cobalt deposition before hydrogen deposition according to the Nernst equation. During the experiment, H(I) and Co(II) competed for discharge as Co(II) was consumed. On the cathode, a dense cobalt coating that can be easily separated from the substrate was formed by adjusting the concentration ratio of Co(II) and H(I) to realize the separation and recovery of cobalt in spent cemented carbide.

As scanning proceeded during cyclic voltammetry, the oxidation potential of Co increased from 0.356 to 0.383 V, and the oxidation potential became more positive. The reduction potential of Co(II)

increased from 0.525 to 0.540 V, and the reduction potential became more negative. The Co(II) reduction on stainless steel was irreversible.

To further study the number of transferred electrons associated with the reduction peak observed by cyclic voltammetry, the scan at 120 mV/s was taken as an example, and 4 points [12] were selected on the right side of the reduction peak, as shown in Table 1.

Table 1. The data of the select points in the cyclic voltammetry (120 mV/s)

I_p/mA	1.007	1.007	1.007	1.007
I/mA	0.991	0.994	0.996	0.998
E/V	-0.508	-0.511	-0.513	-0.516
lg[(I_p-I)/I]	-1.779	-1.859	-1.945	-2.037

On the basis of the data in Table 1, the relationship diagram of E-lg[(Ip-I)/I] was plotted, as shown in Fig. 3.

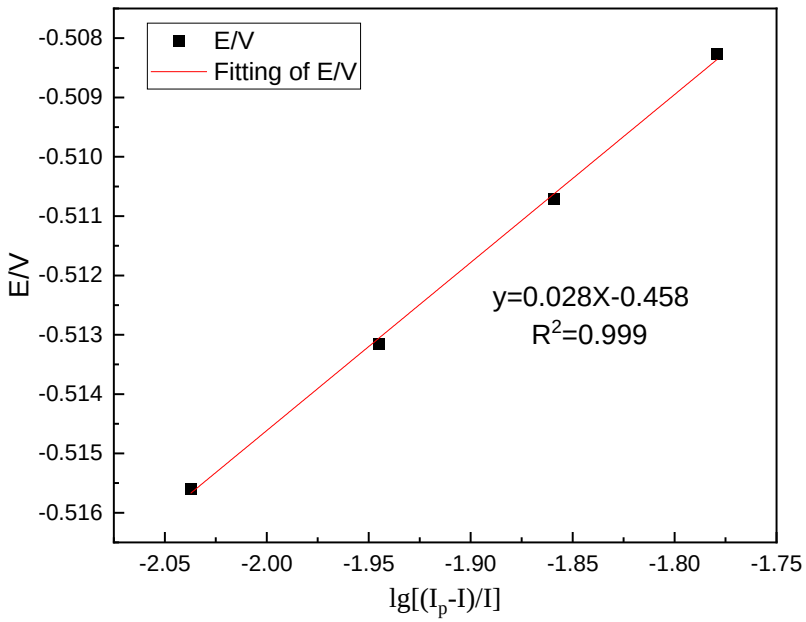

Figure 3. The relationship of E-lg[Ip-I]/I (120 mV/s) in cyclic voltammetry (120 mV/s)

It can be seen from Fig. 3 that the E-lg[(Ip-I)/I] curve has a good linear relationship, and the slope of the line is K=0.028. According to the formula $E = Y + \frac{1.857RTlg\left[\left(Ip-I\right)/I\right]}{nF}$ and the slope $K = \frac{1.857RT}{nF}$ [13], it can be seen that the reduction peak of the cyclic voltammetry at 120 mV/s corresponds to Co(II) in stainless steel. The number of transferred electrons on the electrode is

$n = \frac{1.857 \times 8.314 \times 297}{96500 \times 0.028} = 1.70 \approx 2$. This proves that the reduction process is an irreversible one-step two-electron process. This is the same as the conclusions and results of Jianmin Lin [14] and Xiaoli Xi [10].

To study the control steps and the charge transfer coefficient in the reduction [15-16], the relationship between the scanning rate and peak current and peak potential was plotted, as shown in Fig. 4, and the data are calculated in Table 2.

Table 2. Corresponding parameters of cyclic voltammetry under different scanning rates

v/mV· s^{-1}	0.100	0.105	0.110	0.115	0.120
lnv/ln(V/s)	-2.304	-2.254	-2.207	-2.163	-2.120
$v^{1/2}/(V/s)^{1/2}$	0.316	0.324	0.332	0.339	0.346
E_{pc}/V	-0.525	-0.528	-0.533	-0.538	-0.540
$-I_{pc}$/mA	0.836	0.921	0.949	0.976	1.007
$-E_{pa}$/V	-0.356	-0.371	-0.373	-0.380	-0.383
I_{pa}/mA	0.227	0.311	0.343	0.375	0.410
ΔE_p/V	0.881	0.898	0.906	0.918	0.923
$E_{p/2}$/V	-0.085	-0.079	-0.080	-0.079	-0.079
$\lvert E_{pc}-E_{p/2}\rvert$/V	0.441	0.449	0.453	0.459	0.461
α	0.054	0.053	0.053	0.052	0.052

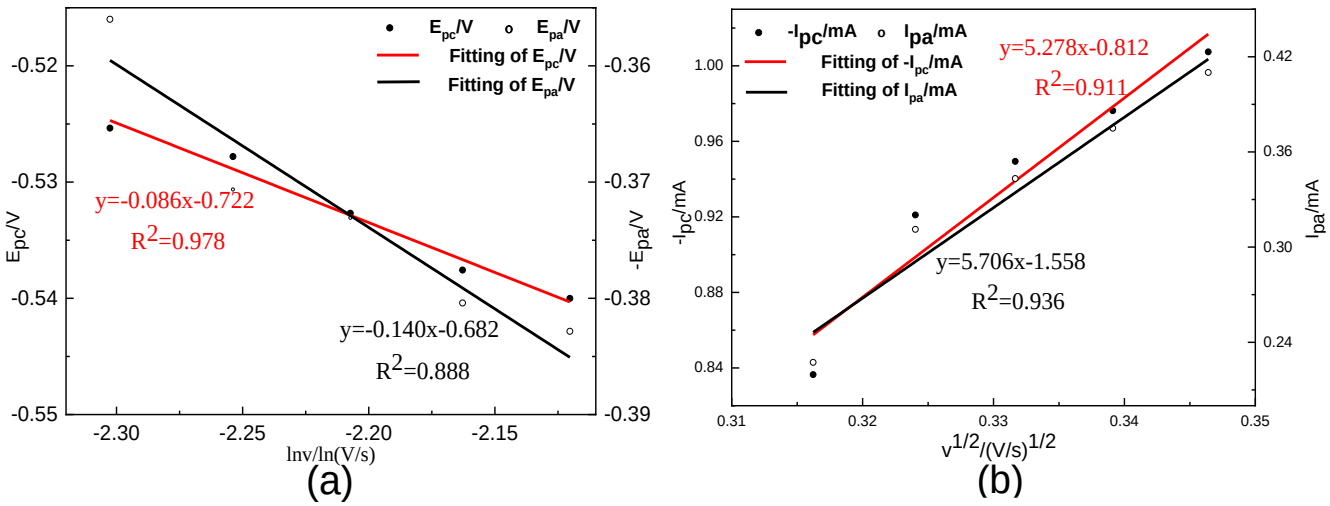

Figure 4. (a) The relationship between the scanning rate and reduction peak potential in cyclic voltammetry; (b) the relationship between the scanning rate and reduction peak current in cyclic voltammetry

Table 2 shows that ΔE_p increases with increasing scanning rate and that the peak current is asymmetrical on the cathode and anode. As shown in Fig. 4(a), E_p is linearly related to lnv but not in a horizontal manner, and in Fig. 4(b), I_p is proportional to $v^{1/2}$. These results prove that Co(II) reduction is an irreversible one-step two-electron process. In irreversible systems, the relationship between the peak potential and the half-peak potential of the cathode conforms to equation (1) [8,12,17].

$$| E_{pc} - E_{p/2}| = \frac{1.857\mathrm{RT}}{\alpha nF} \qquad (1)$$

where E_{pc} is the cathode peak potential (V), $E_{p/2}$ is the half-peak potential (V), α is the charge transfer coefficient, n is the electron transfer number n=2, F=96485 C· mol^{-1}, R=8.314 J· $(mol·K)^{-1}$, and T is the temperature (K).

By substituting the corresponding values into equation (1), the charge transfer coefficient α is calculated to be 0.054, 0.053, 0.053, 0.052, and 0.052, as shown in Table 1, with an average value of 0.053. In Fig. 3, I_P is proportional to $V^{1/2}$, which directly proves that the reduction process is controlled by the diffusion step according to the Berzins-Delahay equation [18-19].

$$I_{pc} = 0.4958nFSC_0\left(\frac{\alpha nvFD_{Co(II)}}{RT}\right)^{\frac{1}{2}} \qquad (2)$$

where I_{pc} is the cathode peak current (mA), n is the electron transfer number, F=96485 C·mol^{-1}, R=8.314 J·$(mol·K)^{-1}$, T is the temperature (K), α is the charge transfer coefficient, S is the working electrode surface area (cm^2), C_0 is the concentration of Co(II) (mol·cm^{-3}), v is the scanning rate (mV·s^{-1}), and $D_{Co(II)}$ is the diffusion coefficient ($cm^2·s^{-1}$).

According to equation (2), when $I_p/v^{1/2}$=5.278 mA· s· m V^{-1}, n=2, F=96485 C· mol^{-1}, R=8.314 J· $(mol·K)^{-1}$, T=298 K, α=0.053, S=0.785 cm^2, and C_0=0.05 mol· L^{-1}, $D_{Co(II)}$ is calculated to be 7.12×10^{-7} $cm^2·s^{-1}$.

3.2. Characterization and analysis of anode mud and its calcined products

The cathode product prepared by electrodeposition was verified to be high-purity cobalt in our previous work [8]. The anode mud was divided into two parts. One part was oxidized and fell into the solution due to the anodizing atmosphere, and the other part was attached to the anode of spent cemented carbide. The anode mud was characterized by XRD and SEM. The results are shown in Fig. 5.

In Fig. 5, the XRD characterization shows that there was no cobalt phase in the anode mud. The skeleton metal cobalt in the spent cemented carbide was first oxidized into solution, $Co-2e^{-}=Co(II)$, and then prepared on the surface of the stainless steel cathode, $Co(II)+2e^{-}=Co$. H_2WO_4 was formed from the oxidation of WC on the anode, $WC_{(s)}+6H_2O\text{-}6e^{-}\rightarrow CO_{2(g)}+H_2WO_{4(s)}+10H^{+}$. Jade calculation of the lattice constants of H_2WO_4 in the anode mud yielded values of a=5.22041 Å, b=10.72572 Å, c=5.17553 Å, and α=β=γ=90°, indicating that this material belongs to the orthorhombic system (a=5.2490 Å, b=10.7110 Å, c=5.1330 Å, and α=β=γ= 90°).

H_2WO_4 cannot be discharged directly to obtain tungsten or tungsten coating, and thus, it is necessary to decompose H_2WO_4 into other forms of tungsten. The water and tungsten oxide in H_2WO_4 form a hydrogen bond. Therefore, calcination causes H_2WO_4 to lose water molecules, resulting in oxidized tungsten.

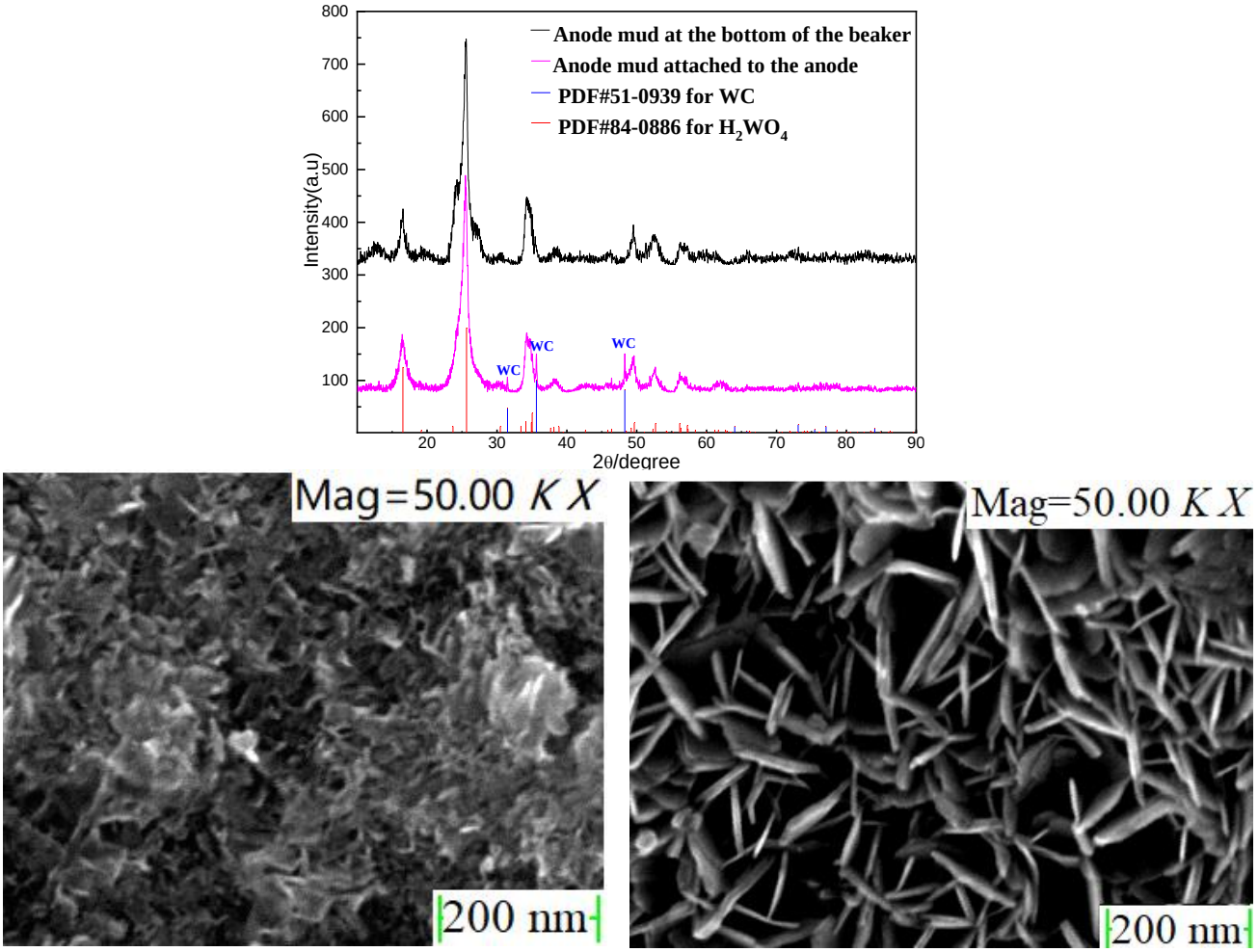

Figure 5. XRD and SEM characterization of the different parts of anode mud

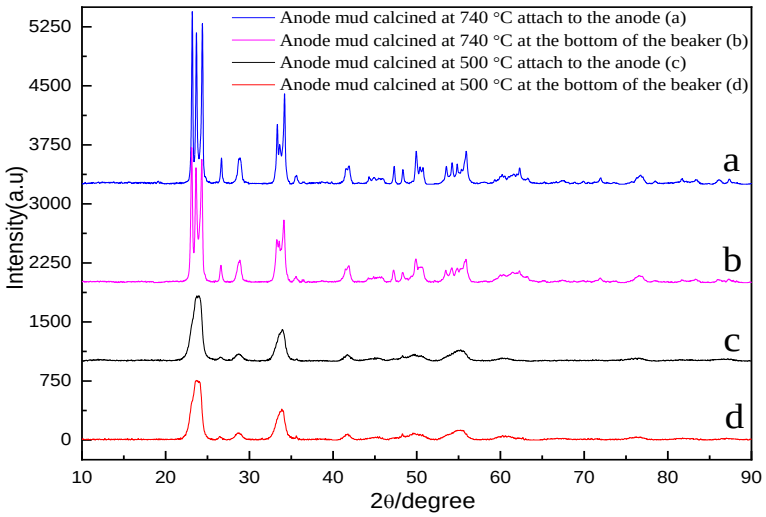

Figure 6. XRD characterization of anode calcined products at 500 and 740 °C

The anode mud was calcined from 500 to 740 °C and then characterized by XRD and SEM. All of the diffraction peaks characterized by XRD correspond to the diffraction peaks in the WO_3 standard card. The diffraction peaks were not marked in Fig. 6 because of density. The XRD results are shown in Fig. 6, and the SEM results are shown in Fig. 7.

In Fig. 6, spectra a and c correspond to the anode mud attached to the anode, and spectra b and d correspond to the anode mud at the bottom of the beaker. The calcination temperature in a and b was 740 °C, while the calcination temperature in c and d was 500 °C, and the calcination time was 8 h. By comparing the XRD characterization results at the same temperature, it can be seen that WO_3 was prepared by calcination, regardless of the source of the anode mud. By comparing the XRD characterization at different temperatures, it can be seen that the WO_3 particles became larger as the temperature increased. The growth mechanism of WO_3 gradually changed from one crystal plane to multiple crystal planes. The WC from the anode mud adhered to the anode disappeared after calcination. The WC underwent oxidation at high temperatures, as described by the following reaction: $WC_{(s)} + O_{2(g)} \xrightarrow{\Delta} WO_{3(s)} + CO_{2(g)}$. No other phase was observed in the XRD characterization, and the purity of WO_3 was relatively high.

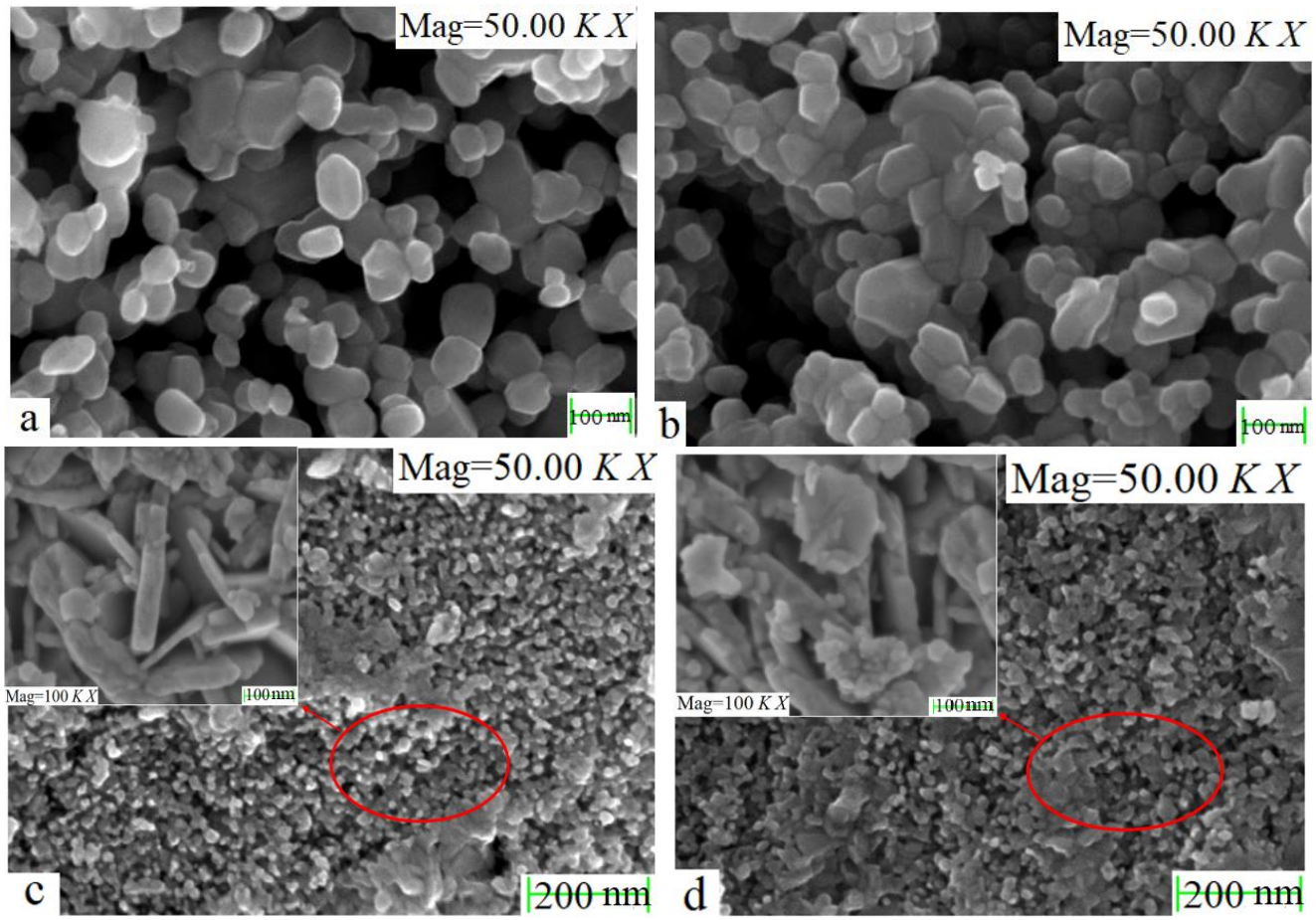

Figure 7. SEM images of WO_3 calcined at 500 and 740 °C

Fig. 7 shows that the morphology and size of WO_3 were related to the temperature. As the temperature increased, the size of the WO_3 particles increased. This result is consistent with the XRD characterization. When the red area in c and d was enlarged by 100 K times, WO_3 was observed to have a sheet-like structure. At higher calcination temperatures, the obtained WO_3 had a relatively regular morphology.

4. CONCLUSIONS

(1). Electrochemical research showed that the deposition potential of Co(II) was between -0.6 and -0.5 V (Vs SCE) and that the reduction mechanism of Co(II) was a one-step two-electron irreversible process. The average charge transfer coefficient was 0.053. The electrodeposition was controlled by the diffusion step, in which the $D_{Co(II)}$ value was 7.12×10^{-7} $cm^2\cdot s^{-1}$.

(2). Product characterization verified that the cathode product was high-purity Co and that the anode mud consisted of H_2WO_4 with a small amount of WC. During calcination, H_2WO_4 was decomposed, and WC was oxidized, which produced high-purity WO_3. High-temperature calcination changed the growth mode of WO_3 from one crystal plane to multiple crystal planes, and the WO_3 obtained consisted of large particles and a more regular morphology.

ACKNOWLEDGEMENTS
This work is supported by the Liaoning Province Natural Science Foundation of China (2019-ZD-0278), the Liaoning University of Science and Technology Graduate Education Reform and Technology Innovation and Entrepreneurship Project (LKDYC201902), the Youth Backbone Talent Project of the University of Science and Technology Liaoning (601011507-11), and the Liaoning Province Talents Program (2017104).

References

1. J.S. Fang, H.M. Wang, C.H. Hsu, Y.L. Cheng and G.S. Chen, *Int. J. Electrochem. Sci.*, 15 (2019) 5143-5153.
2. J. Garcia, V.C. Cipres, A. Blomqvist and B. Kaplan, *Int. J. Refract. Met. Hard Mater.*, 80 (2019) 40-68.
3. T.M. Latha and S. Venkatachalam, *Hydrometallurgy*, 22 (1989) 353-361.
4. Y. Hu, P. Sun, H. Li and A. Chen, *Xiyou Jinshu Yu Yingzhi Hejin*, 32 (2004) 53-57.
5. A. Shemi, A. Magumise, U. Ndlou and N. Sacks, *Miner. Eng.*, 122 (2018) 195-205.
6. P.K. Katiyar and N.S. Randhawa, *Int. J. Refract. Met. Hard Mater.*, (2020) 105251.
7. S. Gurmen and B. Friedrich, *Erzmetall*, 57 (2004) 143-147.
8. H.G. Kang, J.D. Li, C.G. Zhang, J.L. Lu, Q. Wang and Y.Y. Wang, *RSC Adv.*, 10 (2020) 22036-22042.
9. V.M. Lopez-Hirata and E.M. Arce-Estrada, *Electrochim. Acta.*, 42 (1997) 61-65.
10. X.L. Xi, Z.R. Nie, L.W. Zhang and L.W. Ma, *Metall. Mater. Trans. B.*, 48 (2017) 692-700.
11. R.R. Srivastava, J. Lee and M. Bae, *J. Mater. Sci.*, 54 (2019) 83-107.
12. A.J. Bard and L.R. Faulkner, *Surf. Technol.*, 20 (1983) 91 – 92.

13. R.S. Nicholson, *Anal. Chem.*, 37 (1965) 1351-1355.
14. J.M. Lin and H.Z. Wu, *Erzmetall*, 05 (1997) 21-24.
15. M. Li, X.L. Xi and Q. Liu, *J. Electroanal. Chem.*, 833 (2019) 480-489.
16. I. Paseka, *Electrochim. Acta.*, 44 (1999) 4551-4558.
17. Q. Zhang, X.L. Xi, Z.R. Nie, L.W. Zhang and L.W. Ma, *Int. J. Refract. Met. Hard Mater.*, 79 (2019) 145-153.
18. T. Berzins and P. Delahay, *J. Am. Chem. Soc.*, 5 (1953) 555-559.
19. M. Li, Z. Sun, D. Guo, W. Han, Y. Sun, X. Yang and M. Zhang, *Ionics*, 26 (2020) 1-9.